

GFD 2013 Lecture 9: Mass Loss Currents

Paul Linden; notes by Yuki Yasuda and Kate Snow

June 27, 2013

1 Introduction

Previous lectures have investigated the flow of gravity currents where the driving buoyancy is a result of temperature or salinity differences creating a difference in density or stratification between the current and ambient fluid. Another form of gravity current is that in which the difference in density is produced due to suspension of particles in the fluid. The density of the gravity current is then produced from the addition of the fluid and particle densities. Examples of this form of flow include avalanche and pyroclastic flow. For an informative presentation on avalanche flow and a laboratory model set up using sand as the representative particle of the flow, the reader is directed to the website:

<http://www.youtube.com/watch?v=lpjcla-8XNQ>

As a specific example, Figure 1 shows the pyroclastic plume from the 1991 eruption of Mount Pinatubo. Soon after the photo was taken, enough of the particles in the flow had settled out that the hot air of the plume became buoyant enough to rise, allowing the occupants of the vehicle to survive.

Another situation where understanding of this type of flow is important is in industry, for example, water quality and treatment and understanding the removal of unwanted particles in water through sedimentation.



Figure 1: Pyroclastic flow of 1991 Mount Pinatubo eruption.

2 Particle Driven Currents

We will now set up a simple model of a particle driven current which in effect takes the classical gravity current model, but allows for the current density to change due to the deposition of particles. Suppose we have solid particles of density ρ_p suspended in an interstitial fluid of density ρ_i . Assume that $\rho_p > \rho_i$, then it is expected that the particles will fall through the fluid where the falling rate is defined by the Stokes velocity V_s . The Stokes velocity is the terminal velocity at which a sphere of density ρ_p will fall through a fluid of density ρ_i and is dependent on the viscosity, the density difference, gravity g and the size of the particles. In this analysis we assume that all the particles are of the same size and are non-cohesive allowing for a constant V_s to be taken along the length of the current. Further assumptions include:

- The suspension of particles is dilute, which implies there is no hindered settling of the particles.
- The particles are well mixed and only fall out at the lower boundary where the vertical velocity is zero.
- No resuspension occurs.
- The current density and ambient fluid density are similar.

The second assumption is arguable since if it were well mixed, then the flow would be turbulent and detrainment would occur at the top of the fluid. Yet many similar models apply this condition and still provide insightful representations of the flow and little work has been done to verify this assumption for or against. The final assumption given above is suitable for many situation, such as sedimentation or avalanche flow, however fails for cases such as a pyroclastic flow where the hot air of the current is very different from the surrounding ambient. The final assumption also allows the reduced gravity of the current to be defined as:

$$g'_c = \frac{g(\rho_c - \rho_0)}{\rho_0}, \quad (1)$$

where ρ_0 is the density of the ambient and the current density ρ_c is given by:

$$\rho_c = \rho_i + \phi(\rho_p - \rho_i),$$

where ϕ is the volume fraction of particles. Then in the limiting case where $\rho_i = \rho_0$ we get $g'_c = \phi g'_p$ where:

$$g'_p = \frac{g(\rho_p - \rho_0)}{\rho_0}.$$

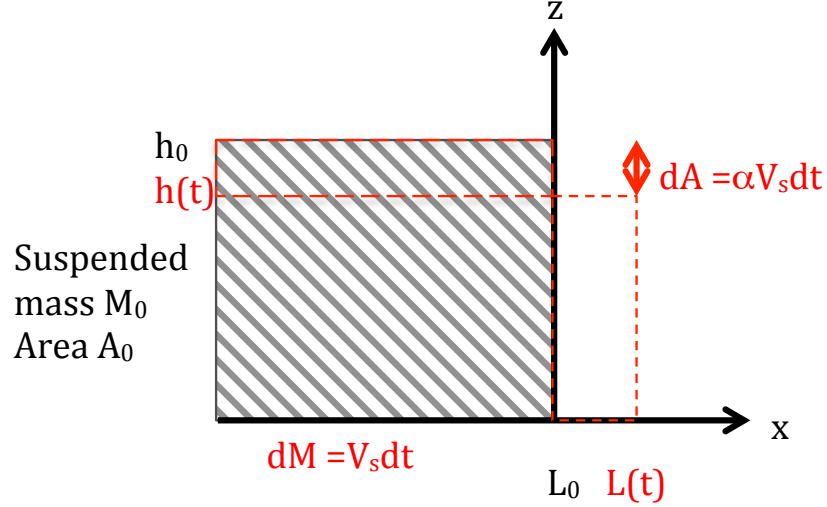


Figure 2: Constant volume release of particle current area A_0 , mass M_0 into ambient fluid.

2.1 Constant Volume Release

We consider the case now of a constant volume release with values defined similarly to previous lectures with the particle current defined over a length $L(t)$ and height $h(t)$ (see Figure 2). We take both the current velocity U and g'_c to be uniform in space and perform the analysis per unit width where width = 1. Then the area of the current is $A = Lh$ and taking M as the suspended mass, the rate of change of mass is given by:

$$dM = -\frac{M}{h} V_s dt = -\frac{M}{A} L V_s dt. \quad (2)$$

To allow for possible entrainment or detrainment at the upper boundary of the current, we also define the rate of change of area of the current:

$$dA = -\alpha L V_s dt, \quad (3)$$

where α defines the degree of entrainment. So if $\alpha = 0$ there is no entrainment and the current remains at a constant volume, if $\alpha > 0$ detrainment of the interstitial fluid occurs and the current volumes decrease and if $\alpha < 0$ entrainment of the ambient fluid occurs increasing the volume of the current. Based on the results of the analysis in previous lectures we also assume here that the propagation occurs with a constant Froude number:

$$dL = F_h (g'_c h)^{\frac{1}{2}} dt. \quad (4)$$

However, though the Froude number is constant, g'_c is not constant but changes with time as particles settle out and so the propagation speed is not constant. In fact, we expect to see the current decelerate with time as particles settle out and g'_c approaches zero. Replacing h with $\frac{A}{L} = \frac{M}{L\rho_p\phi}$ and $g'_c = \phi g'_p$ gives:

$$dL = F_h \left(\frac{g'_p M}{\rho_p L} \right)^{\frac{1}{2}} dt. \quad (5)$$

Taking the initial state as occurring at $L = 0$, $M = M_0$ and $A = A_0$ at $t = 0$, that is, defining the z-axis to be at the initial point of the front of the current, we can use integration of various values to obtain information about the current. So first, divide equation (3) by (2):

$$\frac{dA}{dM} = \alpha \frac{A}{M},$$

which integrates to give:

$$\frac{A}{A_0} = \left(\frac{M}{M_0} \right)^\alpha. \quad (6)$$

Equation (6) indicates the intuitive result that if there is no entrainment ($\alpha = 0$), then the area remains as A_0 but as the entrainment or detrainment increases, the area increases or reduces dependent on the mass and the degree of entrainment. Now to obtain an expression of the length of the flow divide equation (5) with (2):

$$\frac{dL}{dM} = -\frac{F_h}{V_s} \left(\frac{g'_p M}{\rho_p L} \right)^{\frac{1}{2}} \frac{A}{ML},$$

which may be rewritten as:

$$\frac{dL}{dM} = -\frac{F_h}{V_s} \left(\frac{g'_p}{\rho_p} \right)^{\frac{1}{2}} L^{-\frac{3}{2}} M^{-\frac{1}{2}} \left(\frac{M}{M_0} \right)^\alpha A_0, \quad (7)$$

and simplifying:

$$L^{\frac{3}{2}} dL = -c M^{\alpha-\frac{1}{2}} dM, \quad (8)$$

where $c = \frac{F_h A_0}{V_s M_0^\alpha} \left(\frac{g'_p}{\rho_p} \right)^{\frac{1}{2}}$ is a constant. We now integrate (8) to get:

$$\left[\frac{2}{5} L^{\frac{5}{2}} \right]_0^L = -c \left[\frac{M^{\alpha+\frac{1}{2}}}{\alpha + \frac{1}{2}} \right]_{M_0}^M,$$

and putting c back:

$$\frac{2}{5} L^{\frac{5}{2}} = -\frac{F_h A_0}{V_s M_0^\alpha} \left(\frac{g'_p}{\rho_p} \right)^{\frac{1}{2}} \frac{1}{\alpha + \frac{1}{2}} \left(M^{\alpha+\frac{1}{2}} - M_0^{\alpha+\frac{1}{2}} \right),$$

and rearranging:

$$(2\alpha + 1)L^{\frac{5}{2}} = -\frac{5F_h}{V_s} A_0^{\frac{3}{2}} \left(\frac{g'_p M_0}{\rho_p A_0} \right)^{\frac{1}{2}} \left(\frac{M^{\alpha+\frac{1}{2}}}{M_0^{\alpha+\frac{1}{2}}} - \frac{M_0^{\alpha+\frac{1}{2}}}{M_0^{\alpha+\frac{1}{2}}} \right),$$

which gives:

$$\left(\frac{M}{M_0}\right)^{\alpha+\frac{1}{2}} = 1 - (1 + 2\alpha) \left(\frac{L}{L_f}\right)^{\frac{5}{2}}, \quad (9)$$

where we have defined $L_f = \left(\frac{5F_h}{V_s} A_0^{\frac{3}{2}} (g'_0)^{\frac{1}{2}}\right)^{\frac{2}{5}}$ and $g'_0 = \frac{g'_p M_0}{\rho_p A_0}$. But the above equation is only true if $\alpha \neq -1/2$. If $\alpha = -1/2$ we instead get:

$$\frac{M}{M_0} = e^{(-L/\lambda)^{\frac{5}{2}}}, \quad (10)$$

where $\lambda = \left(\frac{5}{2} \frac{F_h}{V_s} A_0^{\frac{3}{2}} (g'_0)^{\frac{1}{2}}\right)^{\frac{2}{5}}$. In this case, since $\alpha < 0$ we have an entraining situation, yet there is no defined limit to this situation, it is seen from equation (10) that the current may go on forever reaching infinite length as the mass becomes smaller and smaller. Clearly this is not a purely realistic situation, yet the results based on the assumptions used are still insightful into the nature of the flow. For example, now consider the case where $\alpha > -1/2$ as defined by equation (9). Simple states for equation (9) would be the $\alpha = 0$ case. Here, the mass becomes zero when $L = L_f$ and we call L_f the run-out length. In other words the current will continue to flow but now only to a finite length defined by L_f . We can also see the dependence of L_f on V_s , indicating that the faster the particles settle out the sooner the current will reach its run-out length.

Now consider the case for $\alpha > 0$. In this case, $(1 + 2\alpha) > 1$, which is effectively equivalent to saying that L_f is smaller as it is an inverse factor in equation (9). In this regime, particles are settling out in addition to loss of volume at the top due to detrainment. This effectively slows down the flow more rapidly.

Figure 3 plots the propagation of the sediment of the non-dimensional time τ , this is the time it would take the flow to reach L_f if no mass were being lost by the current. In the early stages of the flow, the results are equivalent even for the varying amounts of detrainment. One reason for this is that in the early stages of the flow, relatively small amounts of particles have settled out allowing the buoyancy force to be relatively unaffected. However, as the flow continues, more fluid is detrained from the current for the higher values of α , increasing the relative concentration of the particles and so increasing the sediment rate, producing a shorter run-out length, as seen in Figure 3.

The distribution of the sedimentation can also be determined. This is calculated by defining a value $D(x)$ that gives the thickness of the deposit at each distance x along the length of the current. That is:

$$D(x) = - \int_{t_x}^{\infty} \frac{dM}{dt} \frac{1}{L} dt = - \int_x^{L_f} \frac{dM}{dL} \frac{1}{L} dt, \quad (11)$$

where t_x is the time at which the current reaches x . The non-dimensional deposit thickness versus current length are given in Figure 4 for varying values of α . It is seen from this figure, that as the detrainment of the fluid increases, allowing an increased sedimentation rate, the thickness is greater at shorter length but the relative change between values of α is small.

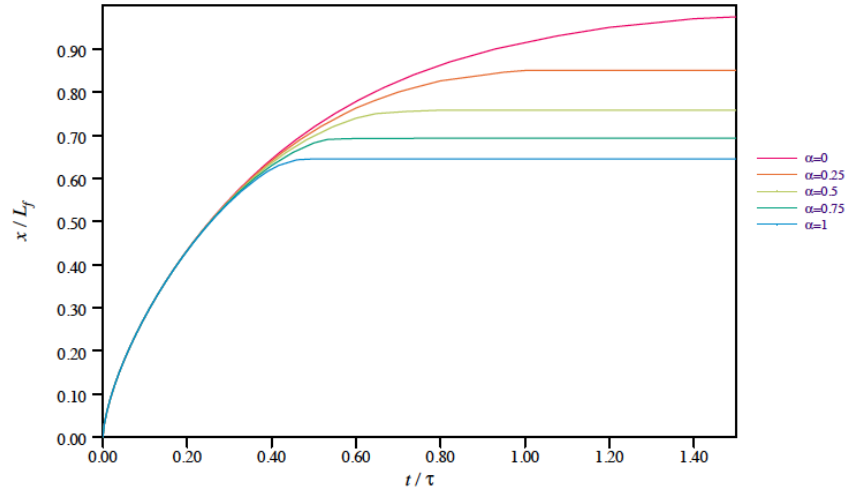


Figure 3: The propagation of the sediment versus time for varying values of α , where time has been non-dimensionalised by $\tau = L_f^{\frac{3}{2}}(g'_0 A_0)^{\frac{1}{2}}$, [3].

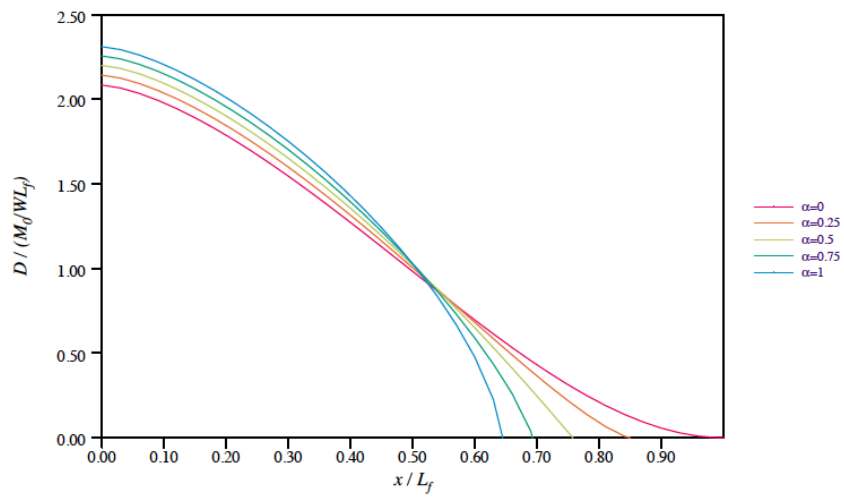


Figure 4: The final sediment distribution versus distance for varying values of α , [3].

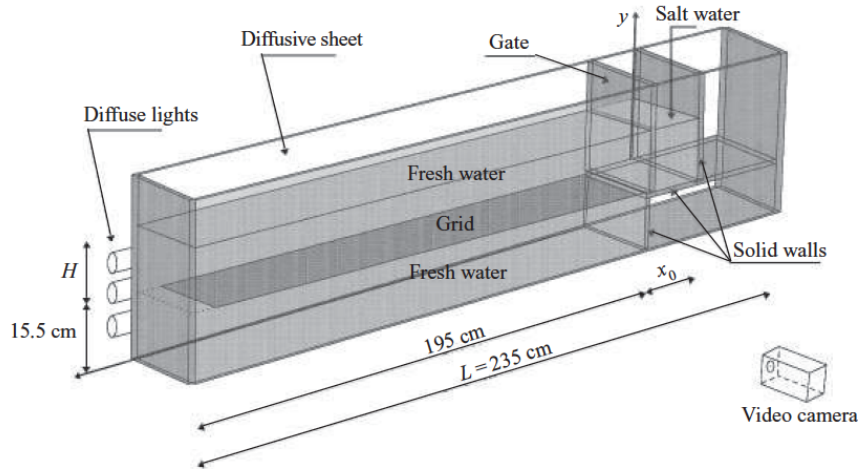


Figure 5: Experimental set-up for the analysis of a gravity current flow over a porous media.

3 Porous Boundary

Another important gravity current situation is the flow over a porous boundary. This may be considered to be similar to the particle-laden fluid current, as the porous boundary acts as a continuous loss of buoyancy of the fluid in a similar manner to the parcel sedimentation of the particle laden fluid. In this case, the flow reduces in density as it flows simply because the denser current is being absorbed by the porous boundary. A representation of the possible experimental set-up of a porous boundary gravity current is given in Figure 5. Further details of this case will refer the reader to [5] and [6].

4 Boundary Currents: Experimentation

In this section, we examine the experimental results of particle-laden gravity currents which are instantaneously released into the homogeneous ambient fluid. This section is based on [3].

4.1 Method to Measure the Thickness of the Sedimentation

For examining the particle-laden gravity currents, it is necessary to measure the sediment layer thickness instantaneously and locally. Here, the thickness of the layer is measured with the use of its electrical resistance. The thicker the sediment layer is, the higher its electrical resistance is. By using this fact, the experimental tank in Figure 6 is used to measure the thickness of the gravity current.

4.2 Results of the Boundary Currents

Experiments of a lock-release gravity currents were performed for various lock aspect ratios (R). Initially, Silicon-Carbide particles were suspended by the water in the lock, and then released instantaneously. Figures 7 shows the time evolution of the gravity current with

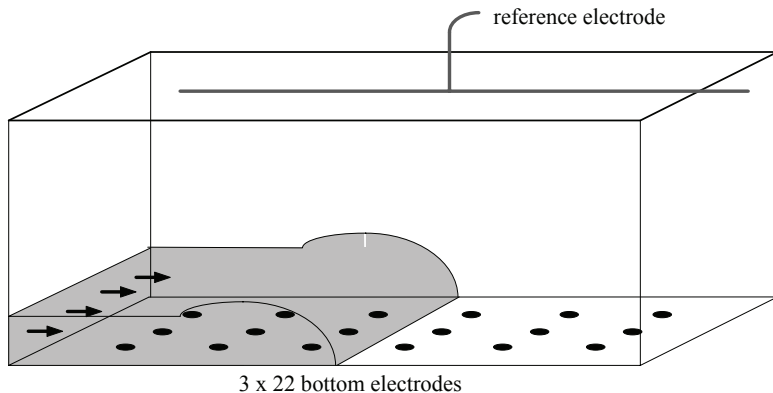


Figure 6: Illustration of the experimental tank to measure sediment thickness. The gray image represents the propagating gravity current.

$R = 0.65$ (low aspect ratio). Each figure shows the image of the current and the plot of the deposit thickness $D(x)$ (defined in (11)).

It is found in this case, that the current has a long tail and the particles are suspended for a long time. Actually, the height of the tail and the magnitude of $D(x)$ are nearly constant until 35 s. After that, a slight maximum can be found near the head of the current.

For the case of the current with the high aspect ratio, instead of the long tail, the current has a short core near the head, and the particles are suspended for a shorter time (not shown).

Figure 8 shows the non-dimensional lengths of currents in the experiments of the four different aspect ratios and the theoretical integral models. Distance and time are non-dimensionalized by using L_f and τ , respectively. The result of the standard integral model corresponds to the experimental data when $R \leq 1.3$. Furthermore, when the dependence of F_h on the current depth is considered, the theoretical prediction becomes closer to the experimental data. However, Figure 8 shows that the current with the highest aspect ratio ($R = 2.6$) is fastest, and the differences between its data and the theoretical predictions grow in time. [4] suggested that the standard integral model underestimates the final length of the current by a factor of 1.6. However, the prediction of this adjusted integral model well corresponds to the experimental data for only $R = 2.6$. The prediction of the integral model with the moving trailing edge ([2]) also well corresponds to the experimental data for $R = 2.6$. This model contains the adjustable parameter C_S , which is set to 1.5, in order to obtain the best fit with the experimental data for $R = 2.6$.

Figure 9a-d show the final sediment distributions for $R = 2.6, 1.3, 0.87$, and 0.65 , respectively. The cases of $R = 1.3, 0.87$, and 0.65 are similar (Figure 9b-d). The large sediment layer thicknesses are observed near the locks, and they decrease monotonically. Their distributions have inflection points and local minimums. However, the case of $R = 2.6$ (Figure 9a) is different from the others. The local minimum is observed near the lock, and the local maximum follows it.

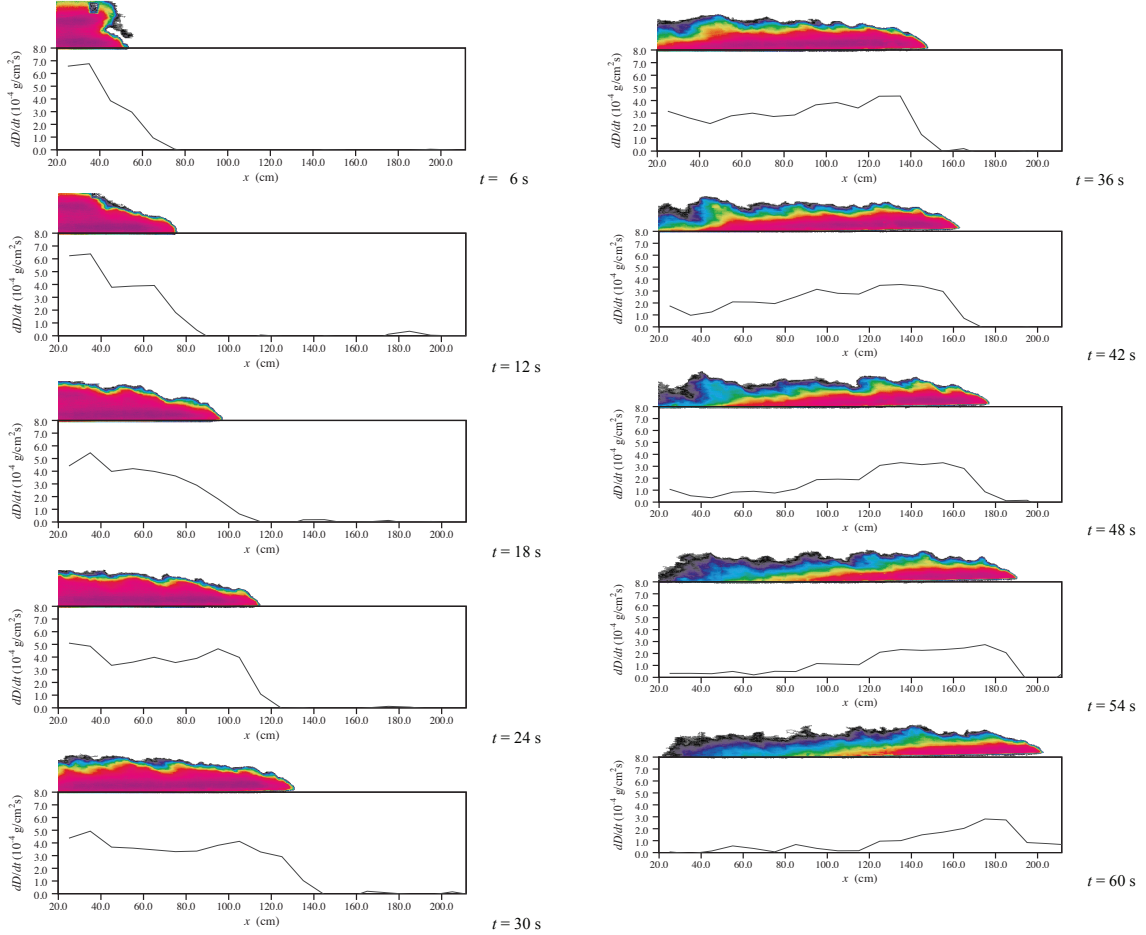


Figure 7: The images of the lock-release particle-laden gravity currents and the plots of its deposit thicknesses $D(x)$. The definition of $D(x)$ is in (11).

Figure 9a-d also show several theoretical predictions. It is found that the result of the standard integral model well corresponds to the experimental data for $R \leq 1.3$ (Figure 9b-d), but not for $R = 2.6$ (Figure 9a). The curve of “shallow water model” is obtained by using the numerical approximation proposed by [1]. Every theoretical model can not predict the local maximum of the current with $R = 2.6$. The only exception is the modified integral model proposed by [2] with the adjustable parameter $C_S = 1.5$ as Figure 8. However, this model has just the local maximum, and its prediction does not correspond to the experimental data (Figure 9a).

The mechanism at which the particles maintaining the initial concentrations reach the front, and then they are deposited is proposed from the following two facts. Firstly, the settling time of the particles ($\frac{h}{V_S}$) is much longer than the speed of the current propagation ($\frac{L_0}{\sqrt{g'h}}$). Secondly, the magnitude of the turbulent velocity for mixing the particles is much smaller than that of the propagation speed. This mechanism is confirmed by using the experimental data. Figure 10a-d show the plots of the deposition rate ($\frac{dD}{dt}$) at various times.

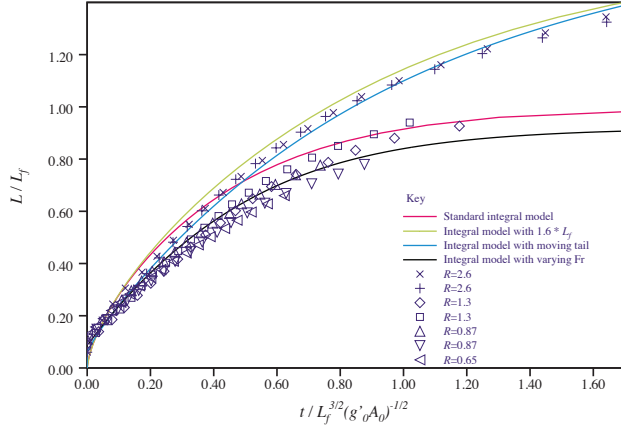


Figure 8: The non-dimensional lengths of the currents for lock-release particle-laden currents. The symbols and curves represent the experimental data and the theoretical predictions, respectively.

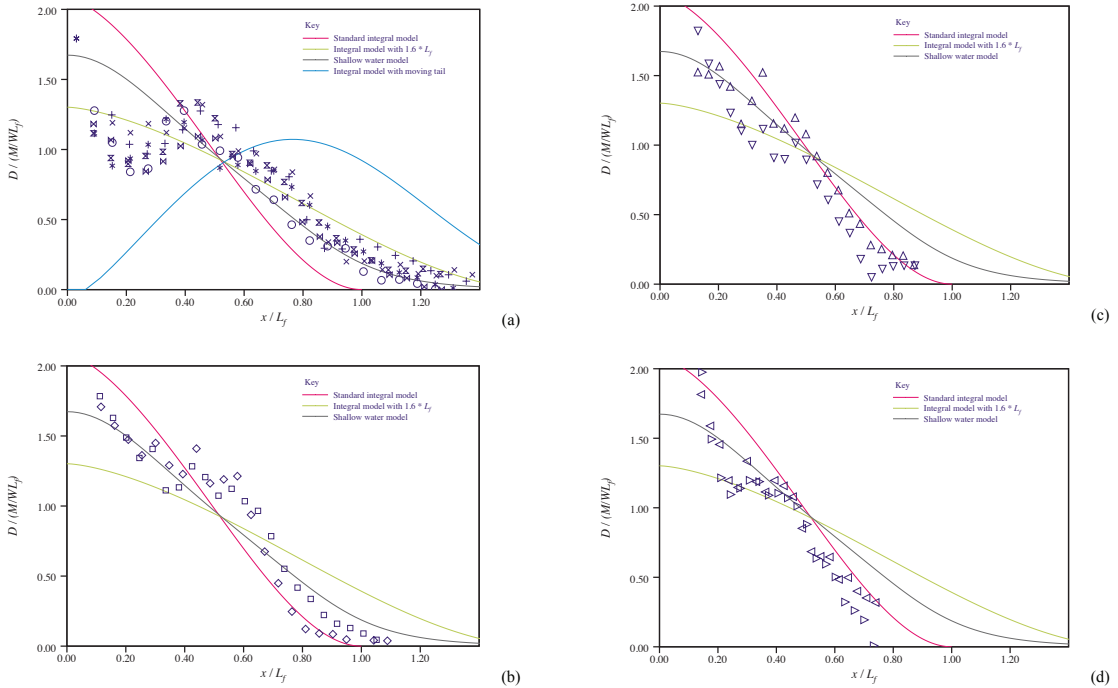


Figure 9: The final sediment distributions for (a) $R = 2.6$, (b) $R = 1.3$, (c) $R = 0.87$, and (d) $R = 0.65$. The symbols and curves represent the experimental data and theoretical predictions, respectively. The deposit thickness and distance are non-dimensionalized.

The purple line represents the expected maximum of the deposition rate from the front

position and above mechanism. It is found that the purple lines well correspond to the instantaneous maximums of the deposition rate.

The integral model with $\alpha = 1$ can express the imperfect turbulent mixing, and then can predict the position $(\frac{L_f}{(2\alpha+1)^{2/5}})$ where the deposition is finished. In Figure 10a-d, the ticks at the top represent these positions. The difference between the experimental data and model predictions is attributed to two facts. First, the location where the magnitude of the deposition begins to decrease is closer to the release position for the experiments than for the models, and second, the models predict abrupt ends of depositing.

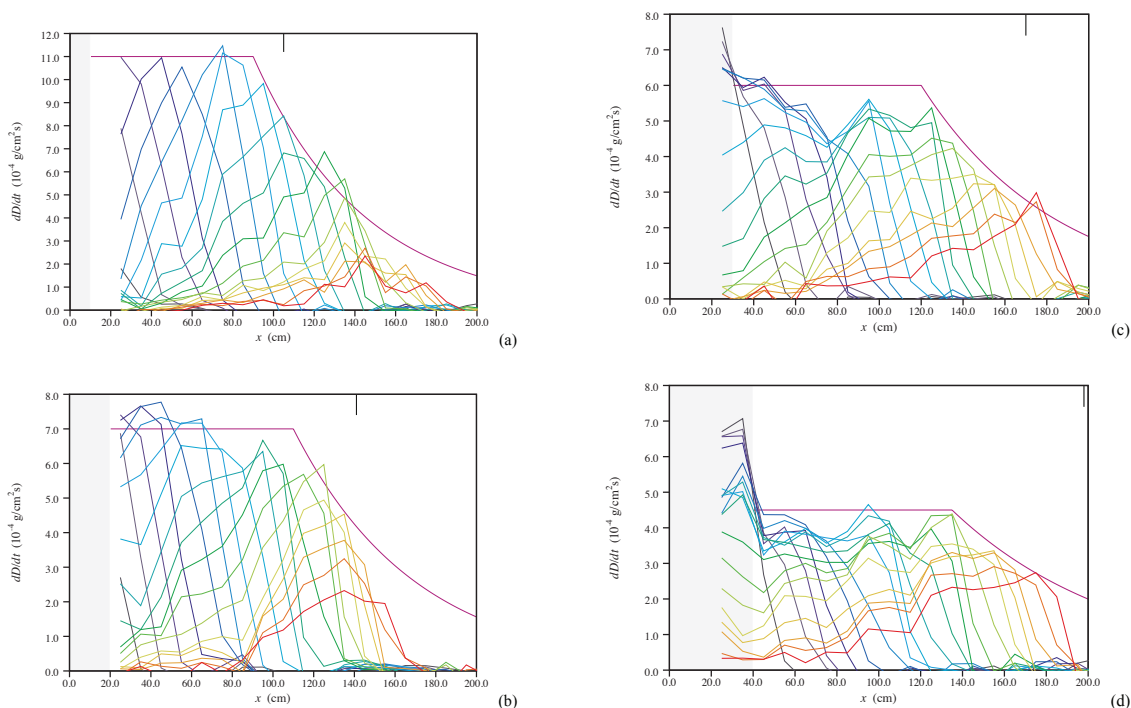


Figure 10: The distributions of the deposition rate ($\frac{dD}{dt}$) at various times for (a) $R = 2.6$, (b) $R = 1.3$, (c) $R = 0.87$, and (d) $R = 0.65$. The time interval is 3 s. The purple line represents the expected maximum of the deposition rate. The tick at the top represents the expected position by the integral model ($\alpha = 1$) where the deposition is finished.

5 Constant-Flux Boundary Currents

In this section, the boundary currents with a continuous release of the particle-laden fluid is examined. Instantaneous deposition were measured by using the system of Section 4.1, as in the preceding experiments. This section is also based on [3].

5.1 Method to Supply Particle-Laden Fluid Continuously

First, we explain how to supply particle-laden fluid continuously. The following system (Figure 11) was used. This system has a particle hopper and a conveyor belt with a scraper, and a constant head tank, which supply the Silicon-Carbide particles and water into the mixing tank at a constant rate, respectively. The particle concentration can be changed by adjusting the speed of the conveyor and the height of the scraper. Fluid is well mixed in the tank, and then supplied into the experimental tank.

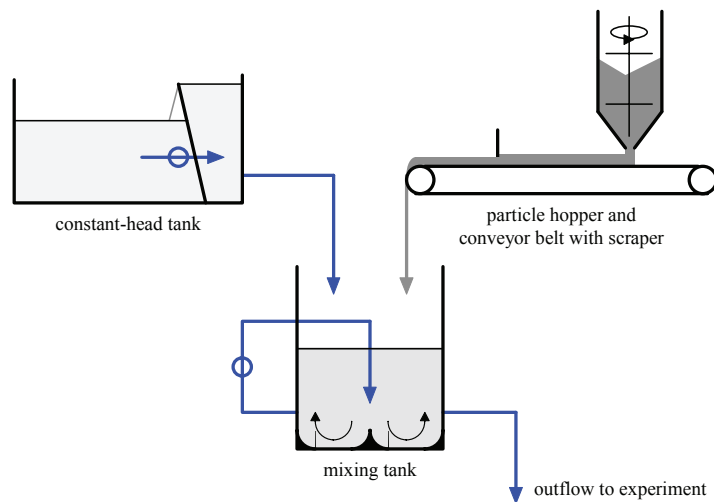


Figure 11: The system supplying the particle-laden fluid continuously.

5.2 Results of the Constant-Flux Boundary Currents

Figure 12 shows the images of the constant-flux particle-laden fluid currents. The color represents the particle concentration. Initially (Figure 12a-f), the front of the current is developed. The concentration near the front gradually decreases due to the deposition, while the concentration near the tail is nearly constant due to the fluid supply. At later time (Figure 12g), the front disappears and the current becomes nearly in steady state. The particle-laden fluid supply maintains the tail in which the particle concentration decreases gradually along the bottom. In addition, the height of the tail is nearly constant in time.

Initially, as the cumulative effects of deposition are small, the buoyancy flux $B = g'Q$ is nearly constant, where $Q(= uh)$ is the volume flux. As the buoyancy drives the current, the speed of the current is also nearly constant (Figure 13). Thus the initial velocity is scaled by $B^{1/3}$. At later time, as the particles are deposited, B decreases. This fact leads to a decrease of the front speed.

Figure 14 shows the plots of the deposition rate. The horizontal extent of the deposition layer increases, as the front propagates further. At later time, as the speed of the front decrease, the curve at each time becomes closer. Figure 14 also shows the plot of the average deposition rate during the steady state. At most locations, the initial deposition

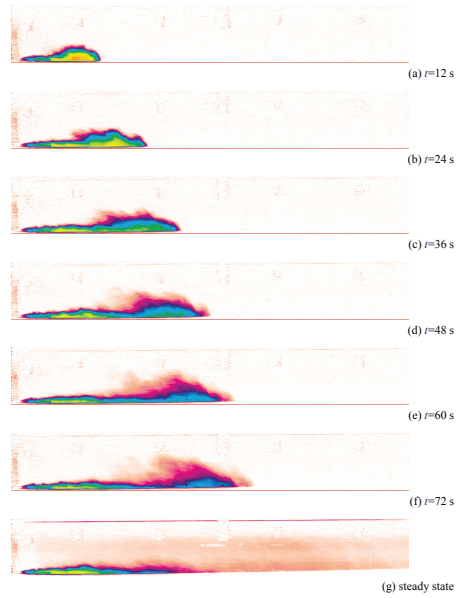


Figure 12: The images of the constant-flux particle-laden fluid currents. The color represents the particle concentration. The time interval is 12 s. (g) shows the current in the first 10 minutes after the start.

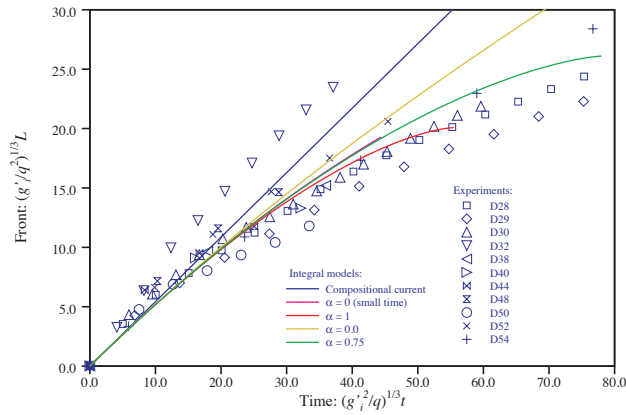


Figure 13: The positions of the fronts plotted against time. The symbols and curves represent the experimental data and model predictions. Distance and time are non-dimensionalized.

rates are higher than the average one. This means that the initial current carries more particles than the steady one.

Finally, we examine the steady state. The steady current can be divided into three zones (Figure 15a). In zone I, the entrainment of the ambient fluid occurs. In zone II, the current

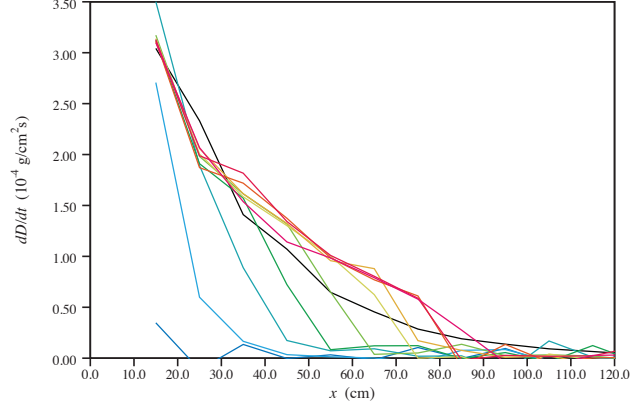


Figure 14: The deposition rates plotted against the horizontal distance for the constant-flux particle-laden fluid currents. The curves are at 12 s intervals. The black curve shows the deposition rate averaged over 5 minutes in the steady state.

has the nearly constant height, and this zone is the longest. Zone III is the extremity of the current, and the height and concentration become zero.

As shown later, the characteristic length scale of zone II depends on the volume flux at the end of zone I (Q_C). Firstly, in order to estimate Q_C , the momentum flux ($F.F.$) at the start and end of zone I is calculated;

$$F.F. := \rho_0 \int_0^h (u^2 + g'z) dz = \rho_0 \left(\frac{Q^2}{h} + \frac{Bh^2}{2Q} \right). \quad (12)$$

Here, the four assumptions were made: (1) Boussinesq approximation; (2) the uniformity of the fluid motion in the layer; (3) the hydrostatic balance because of the approximate horizontality of the fluid motion at the start and end of zone I; and (4) the quite small effects by the ambient fluid ($z = h$ to H).

The entrainment into the layer is characterized by the layer Richardson number (Ri);

$$\text{Ri} := \frac{g'h}{u^2} = \frac{BH^3}{Q^3}. \quad (13)$$

Ri represents the ratio of the magnitude stratification to that of the velocity. (12) can be expressed in terms of Ri;

$$\frac{F.F.}{\rho_0 B^{1/3}} = Q \left(\text{Ri}^{-1/3} + \frac{1}{2} \text{Ri}^{2/3} \right). \quad (14)$$

This quantity is the same at the start and end of zone I. [7] showed that Ri is nearly at unity where the entrainment ceases, i.e., at the end of zone I. Thus, the volume flux at the end of zone I (Q_C) can be expressed as follows;

$$Q_C = Q_I \frac{2 + \text{Ri}_I}{\text{Ri}_I^{1/2}}, \quad (15)$$

where Q_I and Ri_I are the volume flux and Richardson number at the start of zone I, respectively.

By using Q_C , we can estimate the characteristic decay length scale of the particle concentration in zone II. From the observation, h is nearly constant in zone II. This fact suggests that volume flux in zone II is nearly constant and equal to Q_C , and then the horizontal velocity of the current $U(= \frac{Q_C}{h})$ is also nearly constant. In addition, from the visual observation, it is assumed that the current is well mixed and concentration (ϕ) is independent of the height. Thus, we can express the rate of the loss of the particles through the layer as follows;

$$\begin{aligned} h d\phi &= -\phi V_S dt, \\ \frac{d\phi}{dx} &= -\phi \frac{V_S}{Q_C}, \end{aligned} \tag{16}$$

where $U = \frac{dx}{dt}$ is used. From this differential equation, it can be shown that ϕ exponentially decays with a decay length scale $\frac{Q_C}{V_S}$. In Figure 16, the typical decay length scales (λ_{mean}) obtained by the experiments are plotted against the theoretical one $\frac{Q_C}{V_S}$. It can be confirmed that $\frac{Q_C}{V_S}$ represents the typical decay length scale.

In zone II, Ri is between 0.6 and 1.0. This means that the layer is strongly stratified and has a sharp boundary against the ambient fluid. Thus, instability occurs there, which looks like Holmboe shear instability. In Figure 15b, there are waves near the top boundary of zone II corresponding with this instability.

In zone III, as the particle concentration becomes very low, it is difficult to make clear observations. The flow velocity is believed to be too low to maintain the well-mixed current. Thus the steady wedge-shaped extremity is formed. The angle of the wedge (θ) may be calculated from $\theta = \frac{V_S}{U}$, however, we have no experimental data to confirm this.

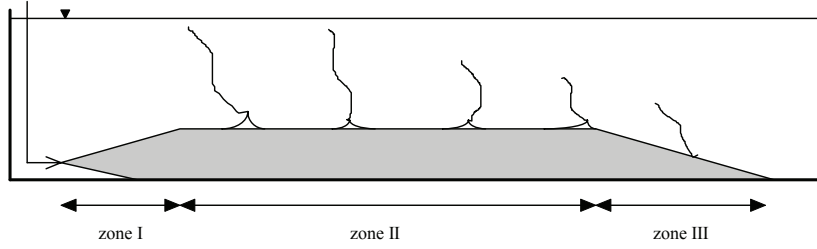
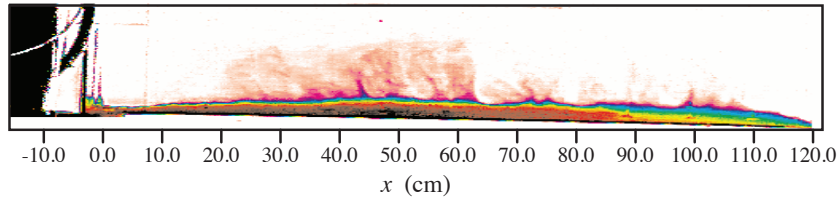


Figure 6.6. Sketch of the steady state reached with a constant flux of particle-laden fluid. The characteristics of the three zones are described in the text.

(a) Figure 15a



(b) Figure 15b

Figure 15: (a) The conceptual illustration for the steady current corresponding to (b). (b) the image of the final steady states. Color represents the particle concentration, and combined dye which is added to visualize Holmboe-like instability near the top of the current.

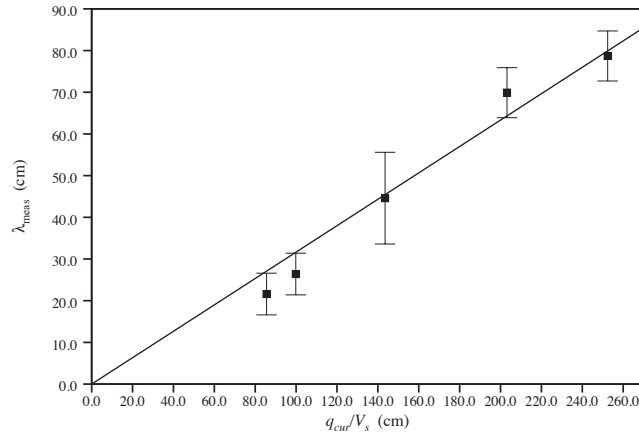


Figure 16: The typical decay length scales (λ_{mean}) obtained by the experiments plotted against theoretical one ($\frac{Q_C}{V_S}$).

References

- [1] R. T. BONNECAZE, H.E. HUPPERT, AND J.R. LISTER, *Patterns of sedimentation from*

- polydisperse turbidity currents*, Proc. Roy. Soc. London A, 452 (1996), pp. 2247–2261.
- [2] W.B. DADE AND H.E. HUPPERT, *Runout and fine-sediment deposits of axisymmetric turbidity currents*, J. Geophys. Res., 100 (1995), pp. 18597–18609.
- [3] F. DE ROOIJ, *Sedimenting particle-laden flows in confined geometries*, PhD thesis, University of Cambridge, 1999.
- [4] H.E. HUPPERT, *Quantitative modelling of granular suspension flows*, Phil. Trans. R. Soc. Lond. A, 356 (1998), pp. 2471–2496.
- [5] L. P. THOMAS, B. M. MARINO, AND P. F. LINDEN, *Gravity currents over porous substrates*, J. Fluid Mech., 366 (1998), pp. 239–258.
- [6] ———, *Lock-release inertial gravity currents over a thick porous layer*, J. Fluid Mech., 503 (2004), pp. 299–319.
- [7] D.L. WILKINSON AND I.R. WOOD, *A rapidly varied flow phenomenon in a two-layer flow*, J. Fluid Mech., 47 (1971), pp. 241–256.